ChemPhysMater 3 (2024) 103–110

Contents lists available at ScienceDirect

ChemPhysMater

journal homepage: https://www.keaipublishing.com/en/journals/chemphysmater/

Research Article

In-situ template etching synthesis of BiON/$BiOCl_{0.9}I_{0.1}$ heterojunction for photocatalytic degradation of tetracycline

Xiaodong Yang[#], Qi Shen[#], Wenwen Cao, Bo Xu[*], Yiqiang Sun[*], Cuncheng Li[*]

School of Chemistry and Chemical Engineering, University of Jinan, Jinan 250022, China

ARTICLE INFO

Keywords:
Heterojunction
Tetracycline reduction
Visible light
Photocatalysis

ABSTRACT

Hierarchical heterostructures have emerged as promising candidates for the efficient photocatalytic degradation of antibiotics owing to their matched energy levels and tunable absorption bands. Herein, we report the facile synthesis of a heterojunction photocatalyst composed of basic bismuth nitrate (BiON) and $BiOCl_{0.9}I_{0.1}$ using a simple room-temperature hydrolysis method. Our results demonstrate that the BiON/$BiOCl_{0.9}I_{0.1}$ composite exhibits superior photodegradation performance compared to pure-phase materials owing to the catalytic enhancement at the heterointerface and the effective separation of the photogenerated carriers. Moreover, the unique three-dimensional microsphere morphology of the synthesized composite enhances its specific surface area and light absorption, further enhancing its photocatalytic activity. In the tetracycline (TC) photodegradation reaction as a model reaction, the catalyst could degrade 88% of TC in just 25 min. Overall, this work provides a promising strategy for the facile and low-cost synthesis of heterogeneous photocatalytic degradation materials.

1. Introduction

Antibiotics are widely used as antibacterial agents and animal growth promoters in the fields of medicine and aquaculture [1–3]. However, the misuse of antibiotics leads to water pollution, which is detrimental to the environment and human health. Moreover, antibiotics are resistant to degradation in traditional sewage treatment methods [4]. Hence, there is a pressing need to develop efficient and environmentally friendly techniques to mitigate the pollution caused by antibiotics [5–7]. Photocatalytic technology, which utilizes sunlight, is considered a promising method for effluent treatment because it is environmentally friendly, requires mild reaction conditions, and involves low energy consumption [8–16]. Photocatalysts can generate potent oxidizing active radicals that break down organic pollutants via transitions between the energy levels of the photogenerated electrons, which are produced upon the irradiating of semiconductors by light [17–20]. The existing photocatalytic oxidation technologies for antibiotic pollutants in water primarily focus on photocatalysts excited by ultraviolet (UV) light [21–23]. However, UV light constitutes only ~5% of the natural light, because of which such catalysts cannot harness the full potential of solar energy. Thus, the development of photocatalysts that can efficiently utilize visible light or the complete solar spectrum is critical for the advancement of photocatalytic oxidation degradation technologies [24–27]. Recently, the research on semiconductor heterojunction photocatalysts has become increasingly prominent. The construction of heterojunction materials can effectively enhance the light response, expand the absorption range to visible light, and prevent the recombination of photogenerated charge carriers [28–34]. Therefore, the construction of heterojunction materials is a promising approach for addressing the narrowband absorption of certain photocatalysts and improving their photocatalytic performance.

Basic bismuth nitrate (BiON), a bismuth-based photocatalyst material, has attracted considerable research attention because of its non-toxicity, low cost, and abundance [35,36]. However, owing to its relatively wide bandgap (3.4–3.6 eV), BiON can only generate carriers under UV irradiation, thereby limiting its photocatalytic activity and practical applications [37,38]. The BiOX structure consists of a periodic arrangement of positively charged $[Bi_2O_2]^{2+}$ and negatively charged halogen layers. The built-in field between the layers can accelerate the separation of photogenerated charge carriers and facilitate the photocatalytic reaction [39–42]. Furthermore, the open interlayer structure of BiOX enables mutual substitution between halogen atoms, leading to the formation of $BiOX_xY_{1-x}$ solid solutions at various halogen concentrations [43–48]. This property allows for the continuous adjustment of the light response over the UV to visible region. Thus, it is essential to develop a new and straightforward method to construct BiON/$BiOX_xY_{1-x}$ composites for photocatalytic reactions by exploiting the advantages of both the materials.

* Corresponding authors.
E-mail addresses: chm_xub@ujn.edu.cn (B. Xu), chm_sunyq@ujn.edu.cn (Y. Sun), chm_licc@ujn.edu.cn (C. Li).
# These authors contributed equally to this study.

https://doi.org/10.1016/j.chphma.2023.08.001
Received 1 June 2023; Received in revised form 24 July 2023; Accepted 4 August 2023
Available online 26 August 2023

Here, we report a simple room-temperature hydrolysis method that uses BiON nanoplates synthesized by a polyvinyl pyrrolidone (PVP)-assisted method as the substrate and different proportions of halogen salts for in situ etching to synthesize three-dimensional (3D) superstructural microspheres assembled from heterogeneous nanosheets. The resultant flower-like structures induced multiple light scattering and reflection effects from the surface, increasing the effective optical path length of the light absorption probability and generating more electron-hole pairs to enhance the photocatalytic activity. The proposed strategy may provide a new approach for synthesizing BiON heterojunctions for the photocatalytic degradation of organic pollutants.

2. Experimental

2.1. Materials

Bismuth nitrate pentahydrate ($Bi(NO_3)_3{\cdot}5H_2O$, 99%), sodium chloride (NaCl, 99%), sodium iodide (NaCl, 99%), ciprofloxacin (CIP, 98%), benzoquinone (BQ 97%), isopropyl alcohol (IPA, 98%), and triethanolamine (TEOA, 99%) were purchased from Sinopharm Chemical Reagent Co., Ltd. PVP (Mw ≈ 360000) was purchased from Sigma-Aldrich. Ethanol (99.9%) was purchased from Xilong Chemical Industry Incorporated Co. Ltd. Ultrapure water (18.2 MΩ cm^{-1}) was used for all the experiments.

2.2. Synthesis of BiON

For the typical synthesis of BiON (i.e., $Bi_6O_5(OH)_3(NO_3)_5{\cdot}3H_2O$), 89 mg of PVP and 194 mg of $Bi(NO_3)_3{\cdot}5H_2O$ were completely dissolved in 8 mL of deionized water by ultrasonication. The solution was then stirred for 12 h to obtain a milky white BiON suspension.

2.3. Synthesis of BiON/$BiOCL_{0.9}I_{0.1}$

For the typical synthesis of BiON/$BiOCl_{0.9}I_{0.1}$, a solution mixture containing 180 μL of 0.1 M NaCl and 20 μL of 0.1 M NaI was added to the prepared BiON suspension under vigorous stirring. After allowing the reaction to proceed for 1 h, the obtained light-yellow BiON/$BiOCl_{0.9}I_{0.1}$ dispersion was centrifuged, washed with ethanol, and dried in a vacuum oven to obtain a light-yellow BiON/$BiOCl_{0.9}I_{0.1}$ powder. $BiOCl_{0.9}I_{0.1}$ could also be obtained by extending the reaction time to 12 h after adding the halogen source.

2.4. Characterization

The samples in the form of crystals were collected and characterized by powder X-ray diffraction (XRD) on a Bruker D8 Advance Automatic Diffractometer using monochromated Cu Kα radiation (λ = 1.5418 Å) at 40 kV and 80 mA. The 2θ scan rate was 5 °/min, and the scan range was 5°–80° The morphology of the samples was characterized by scanning electron microscopy (SEM; FEI QUANTA FEG250) at an accelerating voltage of 20 kV. The lattice structures of the samples were characterized by high-resolution transmission electron microscopy (HRTEM; JEM-2100F) at an accelerating voltage of 200 kV. X-ray photoelectron spectroscopy (XPS; Shimadzu Axis Ultra DLD) was performed to determine the surface electronic states using Al Kα X-ray, with C 1s (284.8 eV) as the reference. N_2 adsorption–desorption isotherms were acquired on a Micromeritics Tristar II 3020 instrument at 77 K. The Brunauer–Emmett–Teller (BET) method was used to calculate the specific surface area based on the adsorption branches. Steady-state photoluminescence (PL) spectra were recorded on a Hitachi F-7000 fluorescence spectrophotometer. The absorption spectra of the solid samples were obtained on a UV–vis diffuse reflectance spectrometer (Perkin Elmer Lambda 950) using $BaSO_4$ as the reflectance sample.

2.5. Photocatalytic testing

In a typical photodegradation experiment, the first step involved stirring 10mg of the catalyst in 99 mL of deionized water to prepare a homogeneous dispersion. Next, a tetracycline (TC) solution was added to achieve a final concentration of 50 mg L^{-1}. The resulting mixture was then stirred in the dark for 20 min to establish an adsorption-desorption equilibrium between the pollutants and catalyst before exposure to visible light. The catalytic performance of the system for degrading TC under visible light irradiation was examined using a 300 W xenon lamp (Perfect Light PLSSXE-300C) as a simulated solar light source. The distance between the lamp and the suspension containing the catalyst and TC was ~25 cm. A circulating water system was employed to maintain a constant reaction temperature of 25 °C and to prevent thermal catalysis. During irradiation, the suspension was sampled every 5 min and the catalyst was separated from the harvested suspension by centrifugation. The residual TC was quantified by recording its UV–vis absorption spectrum after three-fold dilution with deionized water.

2.6. Photoelectrochemical measurements

Photo-electrochemical measurements were performed using a standard three-electrode system. A Pt foil was used as the counter electrode and Ag/AgCl (KCl, 3 M) was used as the reference electrode. The measurements were performed using a Solartron analytical electrochemical analyzer (ModuLab XM). The ITO substrates, which are doped with indium tin oxide, were cleaned in three stages by ultrasonication in distilled water, absolute ethanol, and isopropanol, each for 15 min. Working electrodes were prepared by applying an ethanol-based slurry of the samples (10 mg in 1 mL of ethanol) to clean ITO glass substrates to perform electrochemical impedance spectroscopy (EIS), measure the photocurrent response, and prepare the Mott-Schottky (MS) plots. For the photo-electrochemical measurements, an aqueous 0.5 M Na_2SO_4 solution contained in a quartz cell was used as the electrolyte. The solution was bubbled with N_2 to remove oxygen before performing the measurements.

3. Results and discussion

The morphology of the $BiOCl_{0.9}I_{0.1}$/BiON composite photocatalyst was determined from the transmission electron microscopy (TEM) and SEM images, which revealed a well-dispersed 3D superstructured microsphere composed of nanosheets with a particle size of ~1 μm (Figs. 1(a)(b) and S1). The crystal phase of the composite material was determined by XRD. The composite photocatalyst exhibited characteristic peaks of both BiOCl and BiON (Fig. 1(d)), confirming the co-existence of $BiOCl_{0.9}I_{0.1}$ and BiON in the composite material. The BiON precursor without a halogen source and the $BiOCl_{0.9}I_{0.1}$ sample were reacted for 12 h after halogen addition, and the XRD pattern of the product was analyzed. The XRD pattern did not show any characteristic peak of BiON after the 12 h reaction, indicating the complete conversion of BiON to BiOX. The HRTEM image (Fig. 1(c)) revealed a heterogeneous interface between $BiOCl_{0.9}I_{0.1}$ and BiON in the nanosheets composed of the microspheres. The lattice spacing of BiOCl (0.257 nm) was consistent with its (110) crystal plane, while the lattice spacing of BiON (0.451 nm) was consistent with its (300) crystal face, indicating the successful preparation of the heterojunction catalyst. Furthermore, the mapping images demonstrated that Bi, O, Cl, and I were uniformly distributed in the composite photocatalyst (Figs. 1(e)(f), S2 and S3).

To investigate the mechanism underlying the formation of the 3D microspheres, we conducted time-dependent structural evolution experiments. The TEM images acquired after 0, 20, 40, and 60 min of reaction are shown in Figs. 2(a)–(d). A schematic diagram of the reaction pathway is shown in Fig. 2(e). When bismuth nitrate was introduced into an aqueous solution of PVP, hydrolysis occurred immediately to produce white precipitates with a plate-like morphology (Fig. S4). The resulting

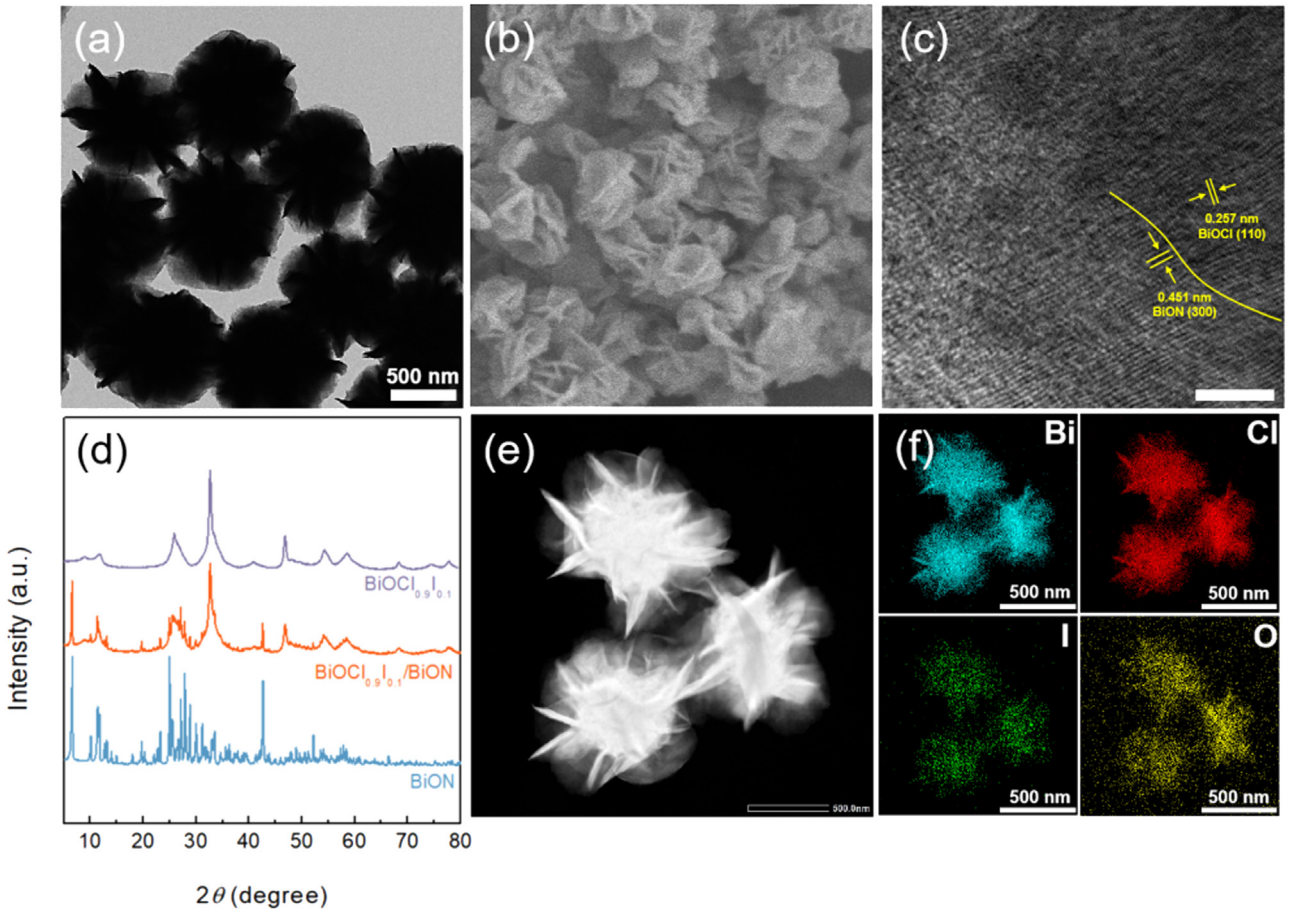

Fig. 1. Morphology and structural characterization of $BiOCl_{0.9}I_{0.1}$/BiON. (a) Low-magnification TEM images, (b) SEM images, (c) HRTEM images, (d) XRD patterns of $BiOCl_{0.9}I_{0.1}$/BiON with different degrees of etching, (e) STEM images, and (f) EDX mapping image of Bi, Cl, I and O.

BiON phase was $Bi_6O_5(OH)_3(NO_3)_5{\cdot}3H_2O$ (JCPDS card No. 70–1226). After the addition of the halogen source, the BiO^- ions on the surface of BiON reacted with Cl^- and I^-, leading to gradual in situ etching of the nanoplates. After 20 min of reaction, the layers of the nanoplates etched by halogen ions began to assemble into 3D microspheres with a hierarchical structure under thermodynamic influence (Fig. S5). As the reaction time increased to 40 min and the stirring became more vigorous, the 3D microspheres began to separate (Fig. S6), eventually leading to the synthesis of the $BiOCl_{0.9}I_{0.1}$/BiON composite comprising flower-like microspheres with uniform size and excellent dispersion (Fig. S7). Prolonging the reaction time to 12 h resulted in the complete etching of BiON by the halogen ions, leading to the formation of a pure-phase $BiOCl_{0.9}I_{0.1}$ solid solution comprising flower-shaped microspheres (Fig. S8).

XPS was employed to investigate the surface chemical compositions and oxidation states of the $BiOCl_{0.9}I_{0.1}$/BiON composite and pure BiON. The obtained binding energy data were corrected using the C 1s spectrum as the reference. The XPS survey spectra of $BiOCl_{0.9}I_{0.1}$/BiON and BiON (Fig. 3(a)) confirm the presence of Bi, O, and N in pure BiON, and Bi, O, N, Cl, and I in $BiOCl_{0.9}I_{0.1}$/BiON. The high-resolution XPS profiles of $BiOCl_{0.9}I_{0.1}$/BiON and BiON in the Bi 4f region (Fig. 3(b)) show that the binding energy shifts to lower values after the BiON nanoplate is etched into the $BiOCl_{0.9}I_{0.1}$/BiON microspheres, indicating strong electronic interactions between the two phases of the composite. Moreover, electrons were transferred from the Cl/I–O–Bi group to the NO–O–Bi group, thereby validating the successful formation of the $BiOCl_{0.9}I_{0.1}$/BiON heterojunction catalyst. As shown in Fig. 3(c), pure-phase BiON exhibited two distinct peaks at 530.9 and 528.7 eV corresponding to the Bi–O bond and O–H bond, respectively, indicating the existing form of oxygen in the basic salt. Following the in situ etching by halogen and the partial transformation into the $BiOCl_{0.9}I_{0.1}$ solid solution, the peak at 528.7 eV was marginally shifted, which could be attributed to the formation of a heterojunction. Meanwhile, the proportion of Bi–O bonds in the O 1s region increased, while that of the hydroxyl oxygen in BiON reduced significantly. Fig. 3(d) presents a comparison of the high-resolution XPS spectra of the N 1s regions of the two phases. For both the samples, two distinct peaks at 406.5 and 399.2 eV were identified, corresponding to the N–O bond in the nitro group and pyridine N on the five-membered ring in PVP, respectively. After the partial in situ etching, the BiON structure was disrupted, and the proportion of the N–O bonds on the surface was substantially lowered, thus confirming the successful synthesis of the composite heterostructure.

The photocatalytic activity of $BiOCl_{0.9}I_{0.1}$/BiON was evaluated using the TC degradation reaction. Comparative analyses were conducted with respect to pure $BiOCl_{0.9}I_{0.1}$, BiON, and $BiOCl_xI_{1-x}$/BiON with varying ratios of chlorine and iodine. Prior to irradiation, the samples were evaluated for pollutant adsorption in the dark. Adsorption–desorption equilibrium was achieved within ~30 min (Fig. S9). Except for the pure BiON phase, all samples exhibited a discernible degree of adsorption for TC. Figs. 4(a) and S10 illustrate that the $BiOCl_{0.9}I_{0.1}$/BiON composite catalyst exhibits the best catalytic ability for the photodegradation of TC under visible light irradiation. The enhanced photocatalytic activity was probably due to the high specific surface area (Fig. S11) and high light absorption ability of the etched 3D microspheres. Notably, $BiOCl_{0.9}I_{0.1}$/BiON exhibited a highly efficient photocatalytic degradation performance for TC compared to previously reported photocatalysts

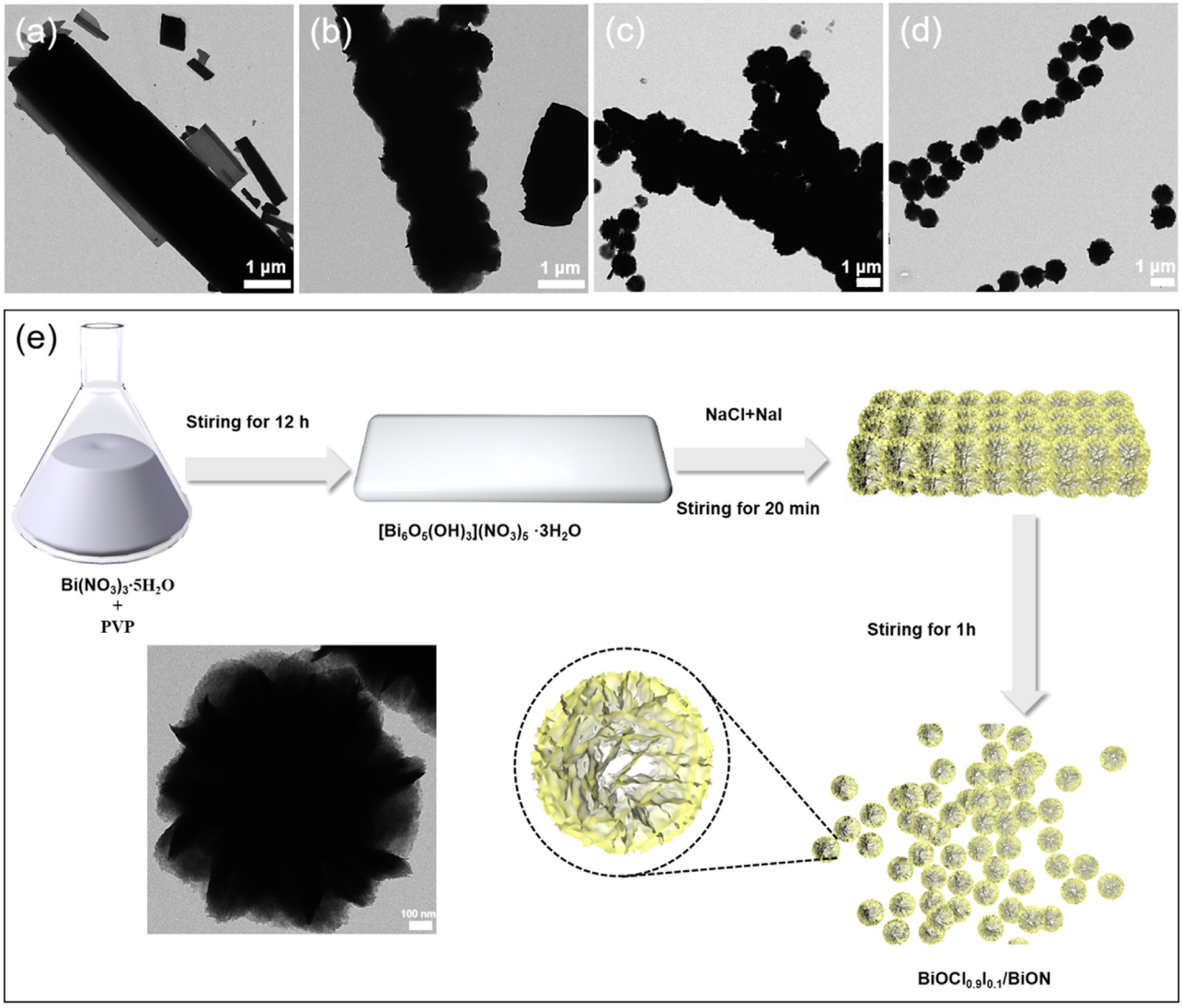

Fig. 2. Reaction pathway and formation mechanism of the $BiOCl_{0.9}I_{0.1}$/BiON composite TEM images of the samples synthesized at different reaction times: (a) 0 min, (b) 20 min, (c) 40 min, and (d) 60 min. (e) Schematic of the synthesis route.

(Table S1). The wide bandgap of the pure-phase BiON renders it challenging to excite the valence band electrons using visible light, thus resulting in negligible catalytic performance. The $BiOCl_{0.9}I_{0.1}$ sample was obtained by the complete etching of BiON with a halogen. However, the BiON phase disappeared during this process, leading to the formation of a $BiOCl_{0.9}I_{0.1}$ solid solution. This transformation, in turn, resulted in the recombination of the photogenerated charge carriers and consequently, poor photocatalytic performance for TC degradation. Under the same test conditions, the $BiOCl_xI_{1-x}$/BiON composition was optimized using different ratios of chlorine and iodine, and $BiOCl_{0.9}I_{0.1}$/BiON was found to exhibit the best catalytic performance (Figs. 4(b) and S12). In addition, to explore the free radical species generated by the samples during the photocatalytic process, the h^+, O^{2-} and –OH active radicals were trapped by TEOA, BQ, and IPA radical scavengers, respectively. Notably, when BQ and TEOA were added to the catalytic system, the catalytic activity of the sample decreased significantly, whereas that of the control group supplemented with IPA showed no significant change (Figs. 4(c) and S13). Thus, h^+ and O^{2-} played a key role in the catalytic process to promote the degradation of TC. We further investigated the visible light-photocatalytic performance under different conditions like varying pH, catalyst dosages, and initial TC concentrations (Figs. S14–S16). TC exists in different forms at various pH values: TC^- at pH ≥ 10, TC^0 at pH = 7.5–10, and TC^+ at pH = 4–7.5. Thus, at pH = 9, the positively charged photogenerated h^+ on the catalyst surface effectively captured and degraded TC, which was present as TC^-. When the pH increased from 3 to 9, the rate of TC degradation increased. However, when the pH increased to 11, the degradation rate started to decrease. During the photocatalytic process, upon the excitation of $BiOCl_{0.9}I_{0.1}$, the h^+ generated in the conduction band acted as an active species to facilitate the oxidation of TC. Hence, an appropriate pH is essential for enhancing the photocatalytic degradation of TC. The influence of catalyst dosage was investigated next. As the catalyst dosage increased, the photocatalytic degradation efficiency of TC improved slightly. However, considering the principles of green chemistry and to ensure its widespread applicability, it is desirable to achieve better degradation with a smaller amount of catalyst. Next, the effect of initial TC concentration was studied. As the concentration of TC increased, the adsorption sites on the catalyst surface were gradually saturated, resulting in decreased binding of TC to the holes and free radicals and consequently leading to a decrease in the degradation rate. Stability is crucial for the application prospects of catalysts and is an important evaluation index. As shown in Fig. 4(d), after three cycles of repeated testing, the performance of the sample did not change significantly, indicating good stability. Furthermore, the phase, BET specific surface area, surface chemical state, and morphology of

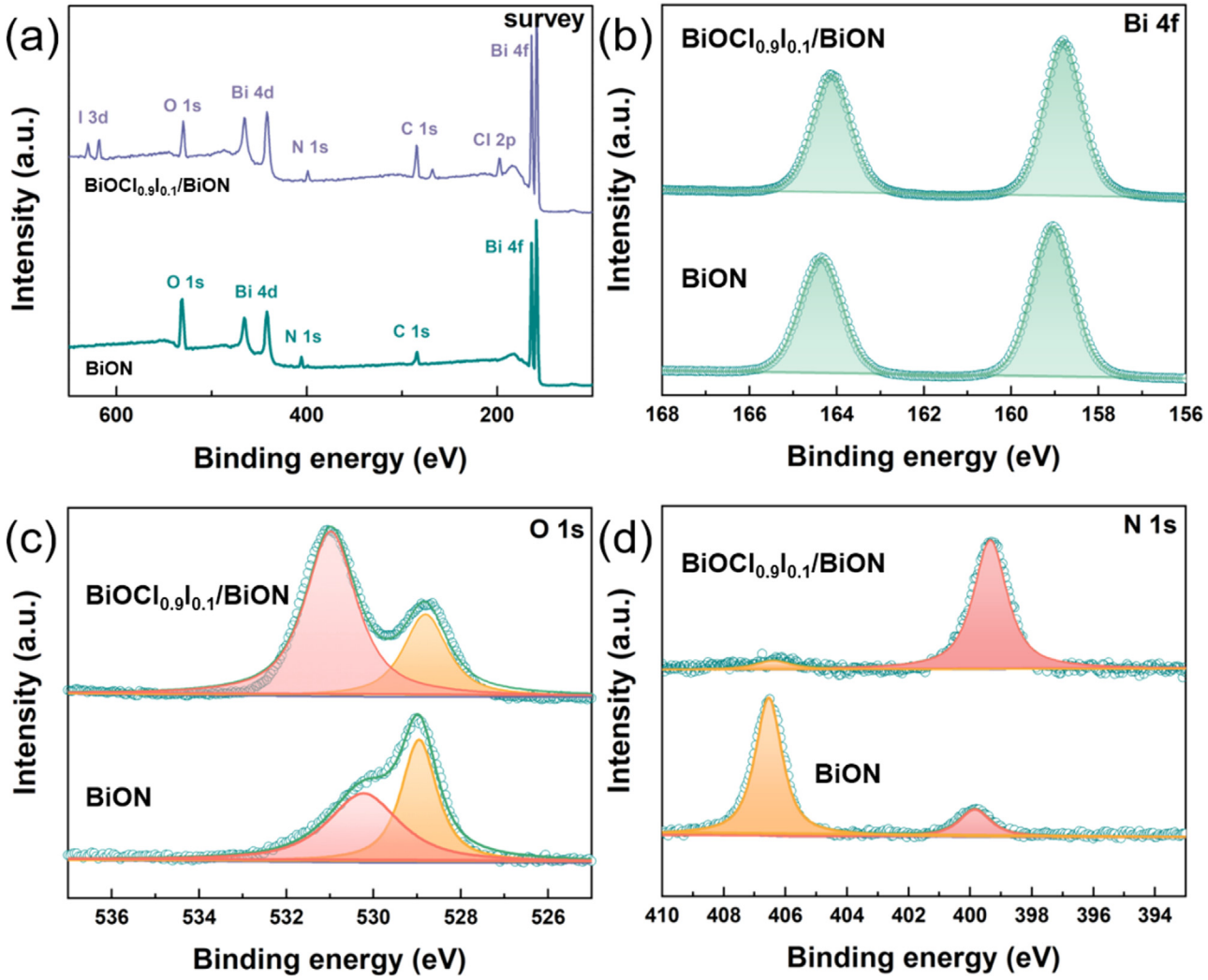

Fig. 3. XPS patterns of $BiOCl_{0.9}I_{0.1}$/BiON and BiON: (a) Full scan spectra, (b) Bi 4f spectra, (c) O 1s spectra, and (d) N 1s spectra.

the catalyst after the stability test (Figs. S17–S21) were examined. The sample retained its original phase, indicating its stability throughout the testing process. Additionally, no significant changes were observed in the specific surface area and morphology of the catalyst after the test.

To further explore the enhanced photocatalytic activity of the $BiOCl_{0.9}I_{0.1}$/BiON heterostructure, its charge separation and transfer were characterized by transient photocurrent spectroscopy and EIS. As shown in Figs. 5(a)(b), the composite material exhibited a higher photocurrent intensity than the pure phase components. Owing to the large bandgap (3.66 eV) of BiON, charge separation under visible irradiation is difficult, which is consistent with its catalytic results. In addition, for solid-solution heterojunction samples with different chlorine–iodine ratios, the photocurrent intensity differed only negligibly. A significant downward trend was observed only at chlorine–iodine ratios less than 8:2. When the chlorine–iodine ratio was greater than 9:1, the photocurrent intensity decreased because of the low BiOI content. The good consistency between the transient photocurrent analysis and catalytic performance confirms that the enhanced photocatalytic activity of the $BiOCl_{0.9}I_{0.1}$/BiON heterostructure toward TC degradation is attributable to its efficient carrier separation. In contrast to that of the pure phases of BiON and $BiOCl_{0.9}I_{0.1}$, the PL of the $BiOCl_{0.9}I_{0.1}$/BiON microspheres was quenched (Fig. 5(c)). This phenomenon indicates that the prepared composite significantly suppressed the photoinduced charge recombination. Time-resolved PL spectroscopy was employed to gain a deeper understanding of the carrier lifetime (Fig. 5(d)). The calculated average lifetime of $BiOCl_{0.9}I_{0.1}$/BiON was found to be 44.9 ns, which is shorter than those of $BiOCl_{0.9}I_{0.1}$ (77.0 ns) and BiON (86.8 ns). The shorter lifetime of $BiOCl_{0.9}I_{0.1}$/BiON can be attributed to the fact that the electrons of $BiOCl_{0.9}I_{0.1}$ initially jumped to the conduction band after being excited and subsequently flowed to the conduction band of BiON. This effective process inhibited the recombination of the photogenerated carriers, thereby decreasing the carrier lifetime. The collective evidence from photocurrent density measurements, transient PL spectra, and time-resolved PL spectra supports the conclusion that the composite $BiOCl_{0.9}I_{0.1}$/BiON catalyst enhances the electron-hole separation efficiency and effectively suppresses their recombination. The electrochemical impedance spectra (Figs. 5(e)(f)) show that the composite material has the minimum internal resistance in the case of visible light irradiation (the visible light intensity is consistent with the photocatalytic activity test), and that the internal resistance of $BiOCl_{0.9}I_{0.1}$/BiON significantly increased in the dark.

Figs. 6(a)(b) show the UV–vis diffuse reflectance spectra (DRS) of pure $BiOCl_{0.9}I_{0.1}$ and BiON, respectively. The absorption onset wavelength of $BiOCl_{0.9}I_{0.1}$ was 467 nm, which was significantly red-shifted compared to that of the BiON precursor (352 nm). This red shift corresponds to narrowing of the bandgap and enhancement of its optical absorption capacity. The optical bandgap of the pure-phase $BiOCl_{0.9}I_{0.1}$ and BiON can be calculated using the following formula:

$$\alpha h\nu = A\left(h\nu - E_g\right)^{n/2},$$

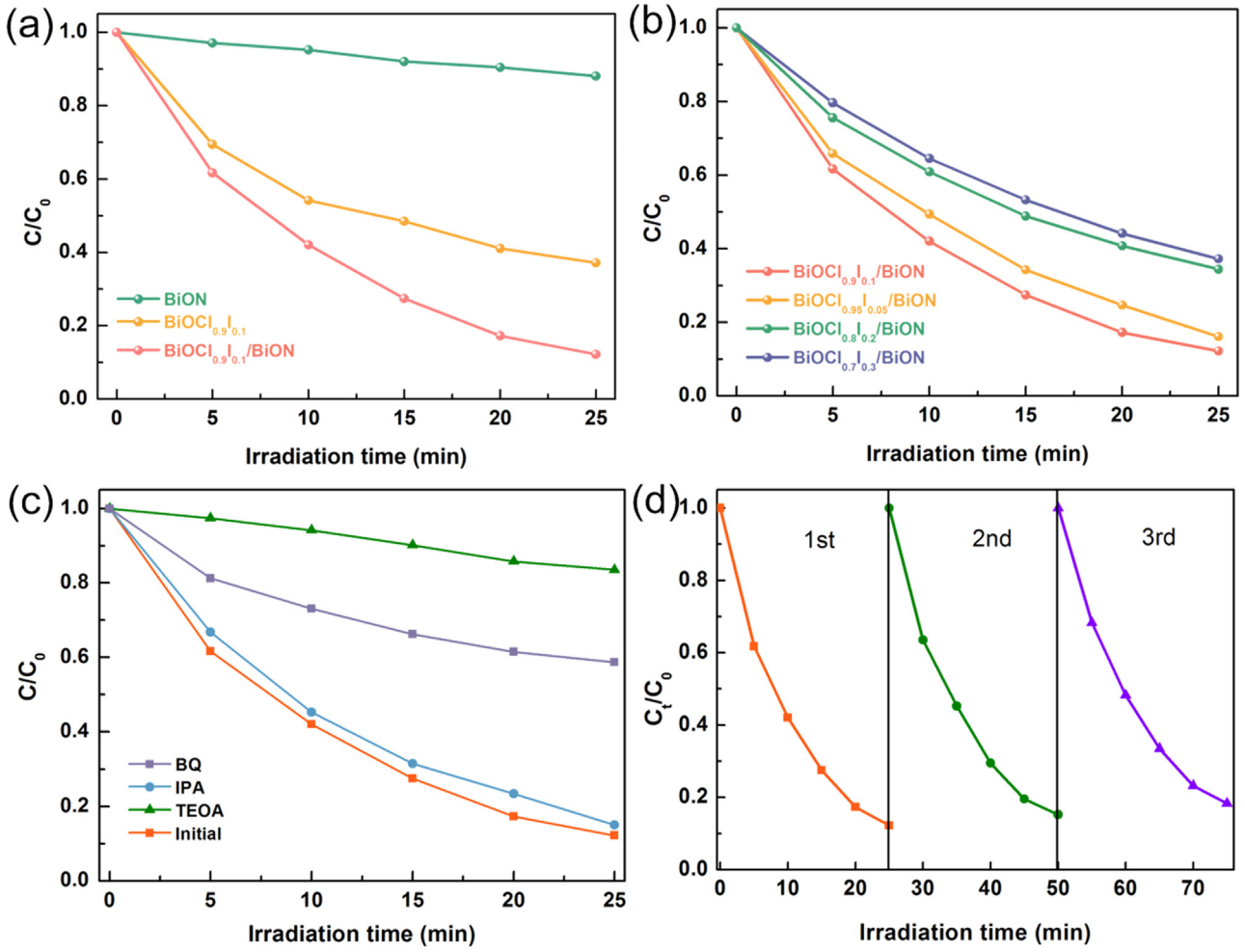

Fig. 4. Photocatalytic performance of various samples. (a) $BiOCl_{0.9}I_{0.1}$/BiON, $BiOCl_{0.9}I_{0.1}$ and BiON and (b) $BiOCl_{0.9}I_{0.1}$/BiON, $BiOCl_{0.95}I_{0.05}$/BiON, $BiOCl_{0.8}I_{0.2}$/BiON, and $BiOCl_{0.7}I_{0.3}$/BiON. (c) Photodegradation efficiency of $BiOCl_{0.9}I_{0.1}$/BiON in the presence of various scavengers. (d) Recyclability of $BiOCl_{0.9}I_{0.1}$/BiON.

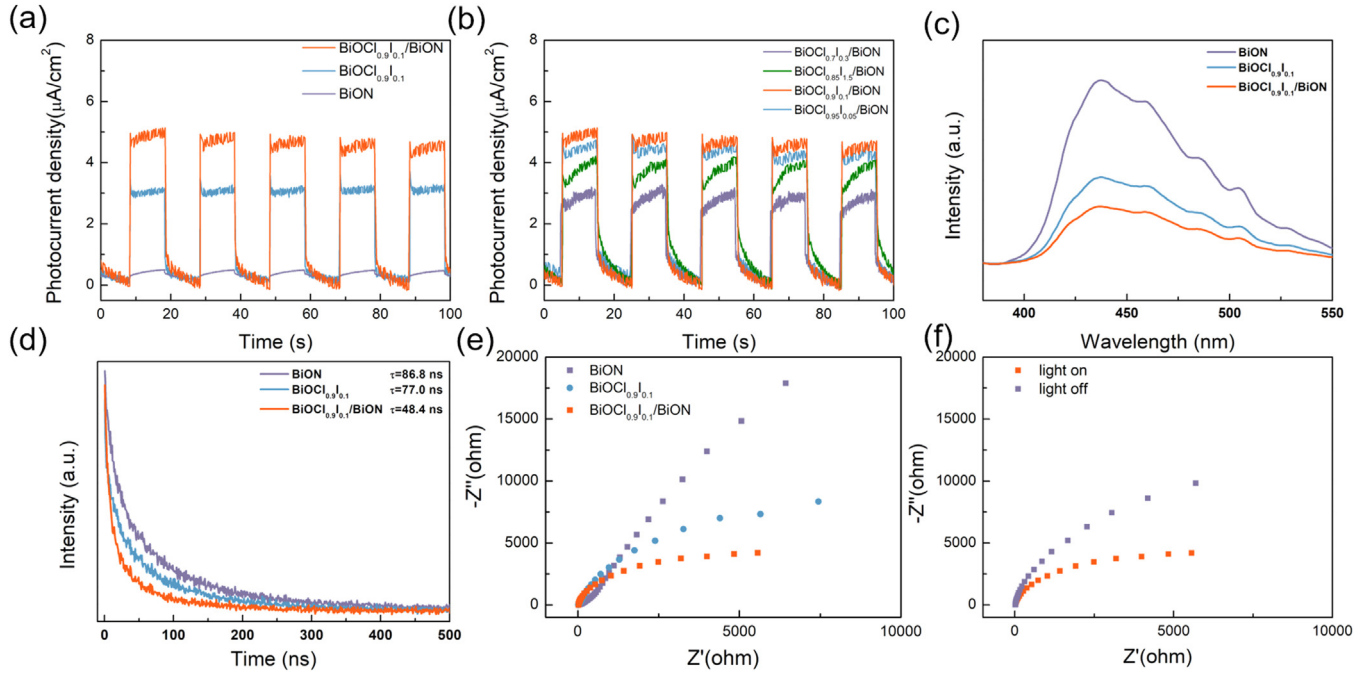

Fig. 5. Photocurrent density under visible light irradiation: (a) $BiOCl_{0.9}I_{0.1}$/BiON, $BiOCl_{0.9}I_{0.1}$ and BiON and (b) $BiOCl_{0.9}I_{0.1}$/BiON, $BiOCl_{0.95}I_{0.05}$/BiON, $BiOCl_{0.8}I_{0.2}$/BiON, and $BiOCl_{0.7}I_{0.3}$/BiON. (c) PL spectra, (d) time-resolved PL spectra, and (e) EIS Nyquist plots of $BiOCl_{0.9}I_{0.1}$/BiON, $BiOCl_{0.9}I_{0.1}$ and BiON. (f) EIS Nyquist plots of $BiOCl_{0.9}I_{0.1}$/BiON under light on/off conditions.

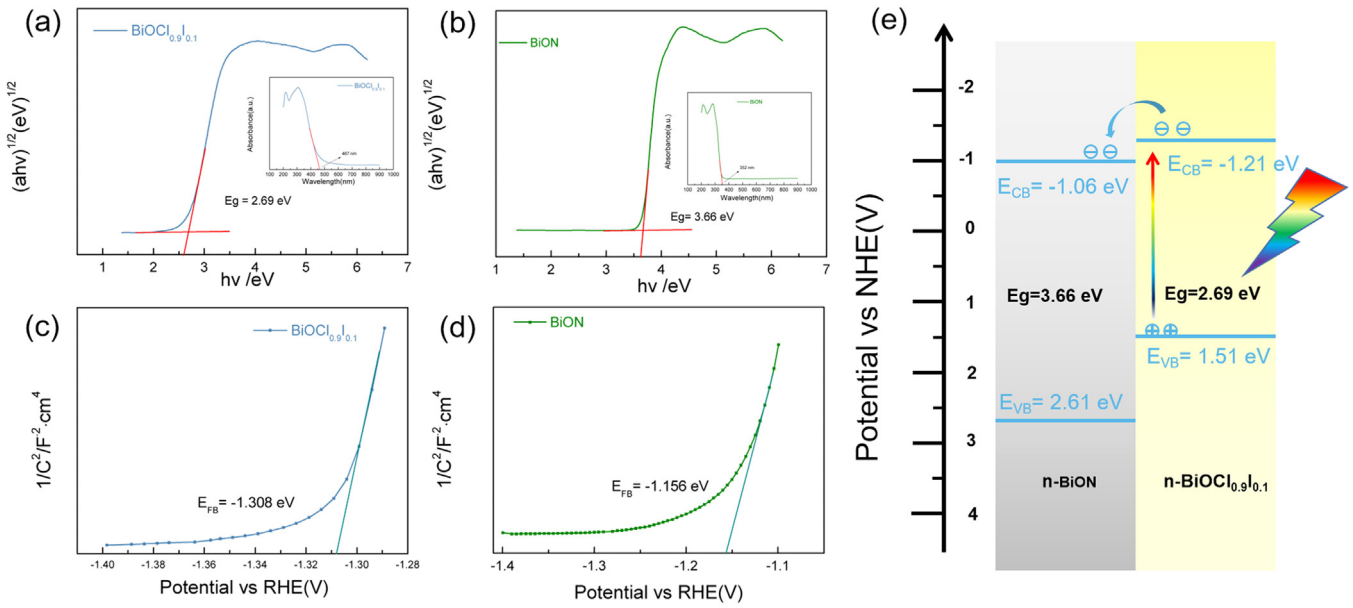

Fig. 6. Derivation of bandgap value of (a) $BiOCl_{0.9}I_{0.1}$ and (b) BiON. (a)(b) represent the respective UV diffuse reflectance spectra. Mott–Schottky plot for (c) $BiOCl_{0.9}I_{0.1}$ and (d) BiON. (e) Schematic diagram of the bandgap structure of $BiOCl_{0.9}I_{0.1}$/BiON.

where α, h, ν, and A represent the absorption coefficient, Planck constant, optical frequency, and proportionality constant, respectively. The optical bandgaps of $BiOCl_{0.9}I_{0.1}$ and BiON were calculated to be 2.69 and 3.66 eV, respectively. The addition of iodide ions to the $BiOCl_{0.9}I_{0.1}$ solid solution endowed it visible light absorption capacity. In addition, the vacuum energy level alignment of the two phases of the heterogeneous samples and the flow direction of electrons and holes upon visible light excitation were investigated. The flat band potentials of $BiOCl_{0.9}I_{0.1}$ and BiON were determined by extrapolating to the infinite capacity C through the Mott-Schottky curve, that is, the linear fitting of $1/C^2$ to 0. As shown in Figs. 6(c)(d), the potentials of $BiOCl_{0.9}I_{0.1}$ and BiON were −1.308 and −1.156 eV. Typically, the position of the conduction band in n-type semiconductors is approximately 0.1 V below the flat band potential. Thus, the conduction band positions were determined to be as follows: $E_{CB,\ NHE}(BiOCl_{0.9}I_{0.1})$ = −1.208eV and $E_{CB,\ NHE}$(BiON) = −1.056 eV. To further validate the accuracy of the band structure, we used the valence band-XPS method to measure the valence band potential ($E_{VB,\ XPS}$). As depicted in Fig. S22, the $E_{VB,\ XPS}$ values for $BiOCl_{0.9}I_{0.1}$ and BiON were 1.39 and 2.49 eV, respectively. E_{VB} of the corresponding standard hydrogen electrode ($E_{VB,\ NHE}$) can be calculated using the formula $E_{VB,\ NHE} = \varphi + E_{VB,\ XPS} - 4.44$, where φ is the work function of the instrument (4.56 eV). Accordingly, the $E_{VB,\ NHE}$ values of $BiOCl_{0.9}I_{0.1}$ and BiON were 1.51 and 2.61 eV, respectively. Assuming that the vacuum is horizontally aligned, the energy band alignment between the two phases, $BiOCl_{0.9}I_{0.1}$ and BiON, of the heterostructure is shown in Fig. 6(e). Under visible light irradiation, $BiOCl_{0.9}I_{0.1}$ undergoes excitation as its bandgap allows the absorption of visible light, leading to the separation of electrons and holes. The excited electrons in the conduction band of $BiOCl_{0.9}I_{0.1}$ then flow to BiON through a self-driven electron-hole flow at the heterojunctions. In the prepared catalytic system, the wide bandgap of BiON prevents its electron-hole separation upon visible light excitation. However, BiON still contributes by providing electrons to the step in the heterojunction, thereby enhancing the electron-hole separation of $BiOCl_{0.9}I_{0.1}$.

4. Conclusion

In summary, $BiOCl_{0.9}I_{0.1}$/BiON microspheres were successfully synthesized by the in situ etching of BiON using a simple room-temperature hydrolysis method, and the mechanism of in situ etching was elucidated through a time-resolved structural evolution experiment. Owing to the heterostructure of the BiON and $BiOCl_{0.9}I_{0.1}$ solid solution, the resultant flower-like composite had a much superior photodegradation performance than the pure-phase materials. The enhanced photocatalytic activity was attributed to the effective separation of the photogenerated carriers by the heterostructures. In addition, the flower-like structures enhanced the light absorption and specific surface area. This study proposes a simple method for constructing bismuth-based heterojunction materials, which may open new avenues for the synthesis of photocatalytic degradation materials.

Declaration of Competing Interest

There are no conflicts to declare.

Acknowledgements

This work was supported by the National Natural Science Foundation of China (Grant Nos. 52001136, 52171179) and the project funded by the China Postdoctoral Science Foundation (2020M671981, 2021T140269).

Supplementary materials

Supplementary material associated with this article can be found, in the online version, at doi:10.1016/j.chphma.2023.08.001.

References

[1] M.M. Fang, J.X. Shao, X.G. Huang, J.Y. Wang, W. Chen, Direct Z-scheme $CdFe_2O_4$/g-C_3N_4 hybrid photocatalysts for highly efficient ceftiofur sodium photodegradation, J. Mater. Sci. Technol. 56 (2020) 133–142.
[2] D. Li, W. Shi, Recent developments in visible-light photocatalytic degradation of antibiotics, Chin. J. Catal. 37 (2016) 792–799, doi:10.1016/S1872-2067(15)61054-3.
[3] T.T. Qian, X.P. Yin, J.H. Li, H.E. Nian, H. Xu, Y. Deng, X. Wang, Nano-TiO_2 decorated radial-like mesoporous silica: Preparation, characterization, and adsorption-photodegradation behavior, J. Mater. Sci. Technol. 33 (2017) 1314–1322.
[4] X. Yang, Z. Chen, W. Zhao, C. Liu, X. Qian, M. Zhang, G. Wei, E. Khan, Y.H. Ng, Y.S. Ok, Recent advances in photodegradation of antibiotic residues in water, Chem. Eng. J. 405 (2021) 126806, doi:10.1016/j.cej.2020.126806.
[5] Z. Wei, J. Liu, W. Shangguan, A review on photocatalysis in antibiotic wastewater: Pollutant degradation and hydrogen production, Chin. J. Catal. 41 (2020) 1440–1450, doi:10.1016/S1872-2067(19)63448-0.

[6] R. Bariki, D. Majhi, K. Das, A. Behera, B.G. Mishra, Facile synthesis and photocatalytic efficacy of UiO-66/$CdIn_2S_4$ nanocomposites with flowerlike 3D-microspheres towards aqueous phase decontamination of triclosan and H_2 evolution, Appl. Catal. B 270 (2020) 118882, doi:10.1016/j.apcatb.2020.118882.

[7] R. Bariki, S. Kumar Pradhan, S. Panda, S. Kumar Nayak, D. Majhi, K. Das, B.G. Mishra, *In-situ* synthesis of structurally oriented hierarchical UiO-66(-NH_2)/$CdIn_2S_4$/$CaIn_2S_4$ heterostructure with dual S-scheme engineering for photocatalytic renewable H_2 production and asulam degradation, Sep. Purif. Technol. 314 (2023) 123558, doi:10.1016/j.seppur.2023.123558.

[8] S. Shurbaji, P.T. Huong, T.M. Altahtamouni, Review on the visible light photocatalysis for the decomposition of ciprofloxacin, norfloxacin, tetracyclines, and sulfonamides antibiotics in wastewater, Catalysts 11 (2021) 437, doi:10.3390/catal11040437.

[9] X. He, T. Kai, P. Ding, Heterojunction photocatalysts for degradation of the tetracycline antibiotic: A review, Environ. Chem. Lett. 19 (2021) 4563–4601, doi:10.1007/s10311-021-01295-8.

[10] R. Ma, Y. Xue, Q. Ma, Y. Chen, S. Yuan, J. Fan, Recent advances in carbon-based materials for adsorptive and photocatalytic antibiotic removal, Nanomaterials 12 (2022) 4045, doi:10.3390/nano12224045.

[11] R. Yang, Z. Zhu, C. Hu, S. Zhong, L. Zhang, B. Liu, W. Wang, One-step preparation (3D/2D/2D) $BiVO_4$/$FeVO_4$@rGO heterojunction composite photocatalyst for the removal of tetracycline and hexavalent chromium ions in water, Chem. Eng. J. 390 (2020) 124522, doi:10.1016/j.cej.2020.124522.

[12] R. Yang, S. Zhong, L. Zhang, B. Liu, PW12/CN@Bi_2WO_6 composite photocatalyst prepared based on organic-inorganic hybrid system for removing pollutants in water, Sep. Purif. Technol. 235 (2020) 116270, doi:10.1016/j.seppur.2019.116270.

[13] Y. Wang, K. Ding, R. Xu, D. Yu, W. Wang, P. Gao, B. Liu, Fabrication of $BiVO_4$/$BiPO_4$/GO composite photocatalytic material for the visible light-driven degradation, J. Clean. Prod. 247 (2020) 119108, doi:10.1016/j.jclepro.2019.119108.

[14] Y. Wang, D. Yu, W. Wang, P. Gao, S. Zhong, L. Zhang, Q. Zhao, B. Liu, Synthesizing Co_3O_4-$BiVO_4$/g-C_3N_4 heterojunction composites for superior photocatalytic redox activity, Sep. Purif. Technol. 239 (2020) 116562, doi:10.1016/j.seppur.2020.116562.

[15] H. Zhang, D. Yu, W. Wang, P. Gao, L. Zhang, S. Zhong, B. Liu, Construction of a novel BON-Br-AgBr heterojunction photocatalysts as a direct Z-scheme system for efficient visible photocatalytic activity, Appl. Surf. Sci. 497 (2019) 143820, doi:10.1016/j.apsusc.2019.143820.

[16] W. Wang, R. Yang, T. Li, S. Komarneni, B. Liu, Advances in recyclable and superior photocatalytic fibers: Material, construction, application and future perspective, Compos. B Eng. 205 (2021) 108512, doi:10.1016/j.compositesb.2020.108512.

[17] H. Tong, S. Ouyang, Y. Bi, N. Umezawa, M. Oshikiri, J. Ye, Nano-photocatalytic materials: Possibilities and challenges, Adv. Mater. 24 (2012) 229–251, doi:10.1002/adma.201102752.

[18] M. Pelaez, N.T. Nolan, S.C. Pillai, M.K. Seery, P. Falaras, A.G. Kontos, P.S. Dunlop, J.W. Hamilton, J.A. Byrne, K. O'shea, A review on the visible light active titanium dioxide photocatalysts for environmental applications, Appl. Catal. B Environ. 125 (2012) 331–349, doi:10.1016/j.apcatb.2012.05.036.

[19] J. Low, J. Yu, M. Jaroniec, S. Wageh, A.A. Al-Ghamdi, Heterojunction photocatalysts, Adv. Mater. 29 (2017) 1601694, doi:10.1002/adma.201601694.

[20] D. Laishram, K.P. Shejale, R. Gupta, R.K. Sharma, Heterostructured HfO_2/TiO_2 spherical nanoparticles for visible photocatalytic water remediation, Mater. Lett. 231 (2018) 225–228, doi:10.1016/j.matlet.2018.08.053.

[21] T.A. Egerton, UV-absorption—The primary process in photocatalysis and some practical consequences, Molecules 19 (2014) 18192–18214, doi:10.3390/molecules191118192.

[22] M. Grandcolas, A. Lind, 3D-printed polyamide structures coated with TiO_2 nanoparticles, towards a 360-degree rotating photocatalytic reactor, Mater. Lett. 307 (2022) 131044, doi:10.1016/j.matlet.2021.131044.

[23] Y. Wang, R. Shi, J. Lin, Y. Zhu, Enhancement of photocurrent and photocatalytic activity of ZnO hybridized with graphite-like C_3N_4, Energy Environ. Sci. 4 (2011) 2922–2929, doi:10.1039/c0ee00825g.

[24] R. Asahi, T. Morikawa, T. Ohwaki, K. Aoki, Y. Taga, Visible-light photocatalysis in nitrogen-doped titanium oxides, Science 293 (2001) 269–271, doi:10.1126/science.1061051.

[25] C. Chen, W. Ma, J. Zhao, Semiconductor-mediated photodegradation of pollutants under visible-light irradiation, Chem. Soc. Rev. 39 (2010) 4206–4219, doi:10.1039/B921692H.

[26] J. Fu, J. Yu, C. Jiang, B. Cheng, g-C_3N_4-based heterostructured photocatalysts, Adv. Energy Mater. 8 (2018) 1701503, doi:10.1002/aenm.201701503.

[27] Z. Zhao, Y. Sun, F. Dong, Graphitic carbon nitride based nanocomposites: A review, Nanoscale 7 (2015) 15–37, doi:10.1039/C4NR03008G.

[28] Z. Xu, Y. Gu, Y. An, C. Zhang, Y. Yu, A. Long, L. Huang, P123-modified synthesis of BiOCl nanosheet/bismuth nitrate heterojunctions for photocatalytic pollutant degradation, ACS Appl. Nano Mater. 5 (2022) 931–938, doi:10.1039/C5CE01787D.

[29] J. Shang, T. Chen, G. Huang, F. Zhou, X. Wang, L. Sun, Oxygen vacancy induced bismuth basic nitrate with excellent photocatalytic activity, J. Mater. Sci. Mater. Electron. 29 (2018) 18067–18073, doi:10.1007/s10854-018-9916-0.

[30] S. Sun, W. Zhou, L. Wang, M. Zhang, I. Lawan, L. Wang, F. Zhang, M. Lin, Z. Yuan, Oxygen-vacancy engineering approach to bismuth basic nitrate/g-C_3N_4 heterostructure for efficiently photocatalytic hydrogen evolution, Int. J. Hydrog. Energy 46 (2021) 25832–25842, doi:10.1016/j.ijhydene.2021.05.098.

[31] X. Hu, L. Cheng, G. Li, One-pot hydrothermal fabrication of basic bismuth nitrate/BiOBr composite with enhanced photocatalytic activity, Mater. Lett. 203 (2017) 77–80, doi:10.1016/j.matlet.2017.05.123.

[32] Y. Ling, Y. Dai, Direct Z-scheme hierarchical WO_3/BiOBr with enhanced photocatalytic degradation performance under visible light, Appl. Surf. Sci. 509 (2020) 145201, doi:10.1016/j.apsusc.2019.145201.

[33] S. Wang, Y. Wang, S.Q. Zang, X.W. David Lou, Hierarchical hollow heterostructures for photocatalytic CO_2 reduction and water splitting, Small Methods 4 (2020) 1900586, doi:10.1002/smtd.201900586.

[34] S. Naghdi, A. Cherevan, A. Giesriegl, R. Guillet-Nicolas, S. Biswas, T. Gupta, J. Wang, T. Haunold, B.C. Bayer, G. Rupprechter, M.C. Toroker, F. Kleitz, D. Eder, Selective ligand removal to improve accessibility of active sites in hierarchical MOFs for heterogeneous photocatalysis, Nat. Commun. 13 (2022) 282, doi:10.1038/s41467-021-27775-7.

[35] S. Gong, Q. Han, X. Wang, J. Zhu, Controlled synthesis of bismuth-containing compounds (α-, β- and δ-Bi_2O_3, $Bi_5O_7NO_3$ and $Bi_6O_6(OH)_2(NO_3)_4{\cdot}2H_2O$) and their photocatalytic performance, CrystEngComm 17 (2015) 9185–9192, doi:10.1039/C5CE01787D.

[36] S. Sun, W. Xiao, C. You, W. Zhou, Z.N. Garba, L. Wang, Z. Yuan, Methods for preparing and enhancing photocatalytic activity of basic bismuth nitrate, J. Clean. Prod. 294 (2021) 126350, doi:10.1016/j.jclepro.2021.126350.

[37] X. Liu, S. Shen, C. Xu, X. Li, L. Zhu, X. Wang, Studying photocatalytic dye degradation with bismuth nitrate–derived catalysts using paper microzones method, Mater. Today Chem. 23 (2022) 100667, doi:10.1016/j.mtchem.2021.100667.

[38] Q. Han, Advances in preparation methods of bismuth-based photocatalysts, Chem. Eng. J. 414 (2021) 127877, doi:10.1016/j.cej.2020.127877.

[39] Y. Zhang, Z. Xu, Q. Wang, W. Hao, X. Zhai, X. Fei, X. Huang, Y. Bi, Unveiling the activity origin of ultrathin BiOCl nanosheets for photocatalytic CO_2 reduction, Appl. Catal. B Environ. 299 (2021) 120679, doi:10.1016/j.apcatb.2021.120679.

[40] J. Li, T. Lu, Z. Zhao, R. Xu, Y. Li, Y. Huang, C. Yang, S. Zhang, Y. Tang, Preparation of heterostructured ternary Cd/CdS/BiOCl photocatalysts for enhanced visible-light photocatalytic degradation of organic pollutants in wastewater, Inorg. Chem. Commun. 121 (2020) 108236, doi:10.1016/j.inoche.2020.108236.

[41] Z. Long, H. Wang, K. Huang, G. Zhang, H. Xie, Di-functional Cu^{2+}-doped BiOCl photocatalyst for degradation of organic pollutant and inhibition of cyanobacterial growth, J. Hazard. Mater. 424 (2022) 127554, doi:10.1016/j.jhazmat.2021.127554.

[42] H. Zhao, X. Liu, Y. Dong, Y. Xia, H. Wang, A special synthesis of BiOCl photocatalyst for efficient pollutants removal: New insight into the band structure regulation and molecular oxygen activation, Appl. Catal. B Environ. 256 (2019) 117872, doi:10.1016/j.apcatb.2019.117872.

[43] M. Kou, Y. Deng, R. Zhang, L. Wang, P.K. Wong, F. Su, L. Ye, Molecular oxygen activation enhancement by $BiOBr_{0.5}I_{0.5}$/BiOI utilizing the synergistic effect of solid solution and heterojunctions for photocatalytic NO removal, Chin. J. Catal. 41 (2020) 1480–1487, doi:10.1016/S1872-2067(20)63607-5.

[44] M. Gao, J. Yang, T. Sun, Z. Zhang, D. Zhang, H. Huang, H. Lin, Y. Fang, X. Wang, Persian buttercup-like $BiOBr_xCl_{1-x}$ solid solution for photocatalytic overall CO_2 reduction to CO and O_2, Appl. Catal. B Environ. 243 (2019) 734–740, doi:10.1016/j.apcatb.2018.11.020.

[45] K. Gao, X. Gao, W. Zhu, C. Wang, T. Yan, F. Fu, J. Liu, C. Liang, Q. Li, The hierarchical layered microsphere of $BiOI_xBr_{1-x}$ solid solution decorated with N-doped CQDs with enhanced visible light photocatalytic oxidation pollutants, Chem. Eng. J. 406 (2021) 127155, doi:10.1016/j.cej.2020.127155.

[46] L. Kong, J. Guo, J.W. Makepeace, T. Xiao, H.F. Greer, W. Zhou, Z. Jiang, P.P. Edwards, Rapid synthesis of $BiOBr_xI_{1-x}$ photocatalysts: Insights to the visible-light photocatalytic activity and strong deviation from Vegard's law, Catal. Today 335 (2019) 477–484, doi:10.1016/j.cattod.2019.02.013.

[47] Y. Gao, W. Yang, X. Shan, Y. Chen, Synthesis of "walnut-like" BiOCl/Br solid solution photocatalyst by electrostatic self-assembly method, Int. J. Energy Res. 44 (2020) 2226–2242, doi:10.1002/er.5084.

[48] L. Qi, Y. Yang, P. Zhang, Y. Le, C. Wang, T. Wu, Hierarchical flower-like $BiOI_xBr_{1-x}$ solid solution spheres with enhanced visible-light photocatalytic activity, Appl. Surf. Sci. 467 (2019) 792–801, doi:10.1016/j.apsusc.2018.10.184.